Transactions of Tianjin University (2021) 27:394–408
https://doi.org/10.1007/s12209-020-00249-5

RESEARCH ARTICLE

Synthesis of Three-Dimensional Hierarchical Flower-Like Mg–Al Layered Double Hydroxides with Excellent Adsorption Performance for Organic Anionic Dyes

Luhong Zhang[1] · Dandan Guo[1] · Xiaowei Tantai[1] · Bin Jiang[1] · Yongli Sun[1] · Na Yang[1]

Received: 31 January 2020 / Revised: 25 February 2020 / Accepted: 10 March 2020 / Published online: 9 May 2020

Abstract

In this work, a facile and effective strategy to prepare three-dimensional (3D) hierarchical flower-like Mg–Al layered double hydroxides (3D-LDH) was developed via a one-step double-drop coprecipitation method using γ-Al_2O_3 particles as a template. The characterization and experimental results showed that the calcined product, 3D-LDO, features a large specific surface area of 204.2 m^2/g, abundant active sites, and excellent adsorption performance for Congo red (CR), methyl orange (MO), and methyl blue (MB). The maximum adsorption capacities of 3D-LDO for CR, MO, and MB were 1428.6, 476.2, and 1666.7 mg/g, respectively; such performance is superior to that of most reported adsorbents. The adsorption mechanism of organic anionic dyes by 3D-LDO was extensively investigated and attributed to surface adsorption, the memory effect of 3D-LDO, and the unique 3D hierarchical flower-like structure of the adsorbent. Recycling performance tests revealed that 3D-LDO has satisfactory reusability for the three organic anionic dyes.

Keywords Layered double hydroxide · Three-dimensional hierarchical flower-like structure · Adsorption · Organic anionic dyes · Mechanism

Introduction

Rapid developments in social industrialization and economic globalization have generated serious environmental pollution. Water pollution caused by organic dyes, in particular, can gravely affect social and ecological development and human health; thus, this issue has aroused great concern [1]. Synthetic dyes are widely used in textiles, printing, plastics, and other industries; unfortunately, dye wastewater is often discharged into the environment without prior treatment [2, 3]. Because most synthetic dyes are toxic and hardly biodegradable, their presence in water, even at very low concentrations, poses harm to humans and the environment [1]. Therefore, research on methods to treat dye wastewater must be undertaken immediately.

Conventional dye wastewater treatment methods mainly include membrane separation [4, 5], chemical oxidation [6, 7], photodegradation [8], and adsorption [9–11]. Among these technologies, adsorption is considered one of the most attractive methods because of its low cost, easy operation, high efficiency, and possibility of material recycling [12–14]. Adsorbents play a significant role in the adsorption process. Various adsorbents, such as activated carbons, zeolite, natural clay materials, and metal oxides, have been studied to remove dyes from aqueous solution [15–19]. However, the low adsorption capacity, weak selectivity, and poor reusability of these materials limit their application [20].

Layered double hydroxides (LDHs) are a class of highly ordered two-dimensional anionic clay materials that have received extensive attention owing to their unique physical and chemical properties, which include a laminar structure, interlayer anion exchangeability, and large specific surface area [20, 21]. LDHs consistently show excellent performance in adsorption applications. Calcination can convert LDHs into mixed oxides (LDO*x*) with large specific surface areas and pore volumes [22]. In addition, LDO*x* has

Electronic supplementary material The online version of this article (https://doi.org/10.1007/s12209-020-00249-5) contains supplementary material, which is available to authorized users.

✉ Na Yang
yangnayna@tju.edu.cn

[1] School of Chemical Engineering and Technology, Tianjin University, Tianjin 300072, China

an inherent and interesting property known as the "memory effect," which means the material can be reconstructed to form the original layered structure of LDHs in the presence of water or aqueous solution containing anions [23, 24]. These properties allow the use of LDO*x* as an adsorbent with very high adsorption capacities. dos Santos et al. [23], for example, reported that the adsorption capacity of calcined LDH for acid yellow 42 is nearly four times greater than that of the original LDH precursor. Zaghouane–Boudiaf et al. [25] demonstrated that calcined MgNiAl-C exhibits a maximum adsorption capacity of 375 mg/g for methyl orange (MO). Despite their many benefits, LDH or LDO powders prepared by conventional methods are prone to aggregation, which severely blocks active sites and limits their adsorption efficiency [26].

Three-dimensional (3D) hierarchical LDH has recently sparked increased interest because its specific surface area and pore volume are higher than those of normal LDH [27]. Dong et al. [28] prepared Ni-Co LDHs with a 3D hierarchical microstructure via a solvothermal method using ethanol. The as-prepared Ni-Co LDHs exhibited a high adsorption rate, large adsorption capacity, and good recycling performance for removing anionic dyes. Xu et al. [29] synthesized hierarchical flower-like Mg_2Al–Cl LDH using a reverse surfactant-free microemulsion route at low-temperature and the calcined product (CLDH) of the flower-like LDH had a large specific surface area of 163.9 m^2/g; the team subsequently found that the as-prepared calcined Mg_2Al–Cl exhibits superior adsorption capacity for MO from aqueous solutions. Zhang et al. [30] synthesized hierarchical organic 3D-LDHs via a one-step hydrothermal strategy using an organic template agent. Zong et al. [31] reported 3D and hollow MgFe-LDO spheres synthesized by sacrificing a carbon template. The hollow MgFe-LDO had a high uptake capability of 398 mg/g toward the anionic dye methyl blue (MB). However, hierarchically structured LDHs prepared by using templates or surfactants to control their morphology via the hydrothermal or solvothermal method may also include heterogeneous impurities [29, 32–37]. In addition, removing the hard template requires complex operations, and the available surfactants are usually toxic organic compounds [38]. Therefore, developing a facile and environment-friendly method for synthesizing pure-phase hierarchical LDHs without any post-processing remains a great challenge.

Herein, we report a facile and efficient strategy to synthesize 3D hierarchical flower-like Mg–Al layered double hydroxides (3D-LDH) via the double-drop coprecipitation method using γ-Al_2O_3 particles as template [39]. The as-prepared 3D-LDO was used as an adsorbent to remove the anionic organic dyes Congo red (CR), MO, and MB from aqueous solution, and the effects of key parameters, including adsorbent dosage, initial dye concentration, contact time, and pH, on the performance of the adsorbent were systematically investigated. The adsorption kinetics, isotherms, and mechanism were also extensively assessed. The experimental results indicated that 3D-LDO exhibits excellent adsorption capability for organic anionic pollutants.

Experimental

Chemicals

γ-Al_2O_3 (size distribution, 20 ~ 40 nm; 99%) was purchased from Aladdin Biochemical Technology Co., Ltd. (Shanghai, China). $Mg(NO_3)_2{\cdot}6H_2O$, $Al(NO_3)_3{\cdot}9H_2O$, CR, and MB were purchased from Tianjin Yuanli Chemical Reagent Co., Ltd. (Tianjin, China). NaOH (98.0%), anhydrous Na_2CO_3, and MO were obtained from Tianjin Kemeiou Co., Ltd. (Tianjin, China). The water used in the experiments was distilled water, and all chemicals used were not further purified. The molecular parameters of the three anionic dyes are listed in Table S1.

Preparation of the Adsorbents

3D-LDH was synthesized by using a double-drop coprecipitation method based on the team's previous research [39]. In a typical synthesis procedure, the appropriate amounts of metallic nitrates (Mg/Al molar ratio, 4) were dissolved in 50 mL of deionized water to produce solution A. Solution B consisted of 0.1 g of γ-Al_2O_3 (ultrasonic treatment for 30 min for dispersion, hydrolysis under suitable alkaline conditions and the Al^{3+} produced by hydrolysis of Al_2O_3 in solution B is used as a partial aluminum source to synthesize 3D-LDH) and 0.636 g of anhydrous Na_2CO_3 as the precipitating agent in 50 mL of deionized water. Solution B was added to a 250-mL round flask, and solution A was added dropwise to this flask at room temperature with vigorous stirring. The pH of the mixture solution was kept constant at 9.2 ± 0.2 by addition of 1 mol/L NaOH aqueous solution. The double-drop process was conducted for approximately 0.5 h. The obtained suspension was aged at 65 °C for 15 h, and the product was filtered, thoroughly washed with deionized water, and then dried at 80 °C for 6 h. Finally, the sample was calcined at 773 K (5.5 K/min) in air for 5 h. The precursor and calcined samples are hereinafter referred to as 3D-LDH and 3D-LDO, respectively.

The synthesis of ordinary hexagonal plate-like Mg–Al LDH was conducted by using the same method employed to obtain 3D-LDH except that solution B was not added with γ-Al_2O_3 particles. The molar ratio of Mg^{2+}/Al^{3+} in the mixed metal salt solution A was 3.01, and the pH was controlled to be 9.2 ± 0.2.

Adsorption Experiments

Batch adsorption experiments were conducted to investigate the adsorption of CR, MO, and MB from aqueous solution onto 3D-LDO. A certain mass of 3D-LDO was added to 50 mL of solution containing a certain dye concentration (50–300 mg/L), and the mixture was stirred at 25 °C under a constant agitation speed of 200 r/min. After achieving adsorption equilibrium, the adsorbent was separated by filtration, and the concentration of the dye remaining in the solution was determined by using a UV–Vis spectrophotometer (UV-4802S, Unico, USA) at maximum absorbance wavelengths of 496, 465, and 594 nm for CR, MO, and MB, respectively. Each experiment was performed in triplicate.

The dye removal efficiency (%), equilibrium adsorption capacity (q_e, mg/g) and adsorption capacity at time t (q_t, mg/g) were calculated according to the following equations:

$$R\% = 100 \times \frac{C_0 - C_e}{C_0} \tag{1}$$

$$q_e = \frac{(C_0 - C_e)V}{m} \tag{2}$$

$$q_t = \frac{(C_0 - C_t)V}{m} \tag{3}$$

where C_0, C_e and C_t are the initial dye concentration, equilibrium dye concentration, and dye concentration at time t, respectively, mg/L; V is the volume of the dye solution, L; and m is the mass of the adsorbent, g.

Recycling Experiment

The recyclability of the adsorbent was investigated by repeated adsorption–calcination cycling using the same 3D-LDO sample. The adsorbent was separated from the mixture solution after adsorption, oven-dried at 80 °C for 6 h, and calcined at 500 °C for 3 h in a furnace. The calcined 3D-LDO was then recycled for the next experiment. This procedure was repeated four times, and the removal efficiencies of the adsorbent after each cycle were calculated.

Adsorbent Characterizations

The crystal structures and compositions of 3D-LDH and 3D-LDO were identified by using an X-ray diffractometer (XRD; BRUKER D8-FOCUS) with Cu Kα ($\lambda = 1.54$ Å) radiation at 40 kV and 40 mA. Scanning was conducted over diffraction angles (2θ) ranging from 5° to 75° with a step size of 8°. Fourier transform infrared spectroscopy (FT-IR) data were acquired on a Nicolet 6700 Fourier transform spectrometer over the spectral range of 4000–500 cm^{-1} using the KBr pellet technique. The morphologies of 3D-LDH and 3D-LDO were observed by field emission scanning electron microscopy (FESEM; Hitachi S-4800, Japan). The specific surface areas of the samples were measured by a Micromeritics ASAP 2020 sorptometer via N_2 adsorption–desorption. The BET method was used to calculate specific surface areas, and the BJH method was employed to determine pore size distributions. The zeta potentials of 3D-LDO under different pH were determined by a Malvern Zetasizer 3000HSA analyzer. The absorption spectra of the initial CR, MO, and MB solutions were obtained by using a UV–Vis spectrophotometer at wavelengths of 496, 465, and 594 nm, respectively, to analyze their concentration in solution.

Results and Discussion

Adsorbents Characterization

Figure 1a illustrates the XRD patterns of 3D-LDH and 3D-LDO. The XRD pattern of 3D-LDH contains the characteristic peaks of 11.32°, 22.84°, 34.58°, 38.93°, 45.95°, 60.41°, and 61.60°, which could be indexed to the (003), (006), (012), (015), (018), (110), and (113) planes of hydrotalcite crystals. The presence of sharp and intense diffraction peaks indicates that 3D-LDH has excellent layered features

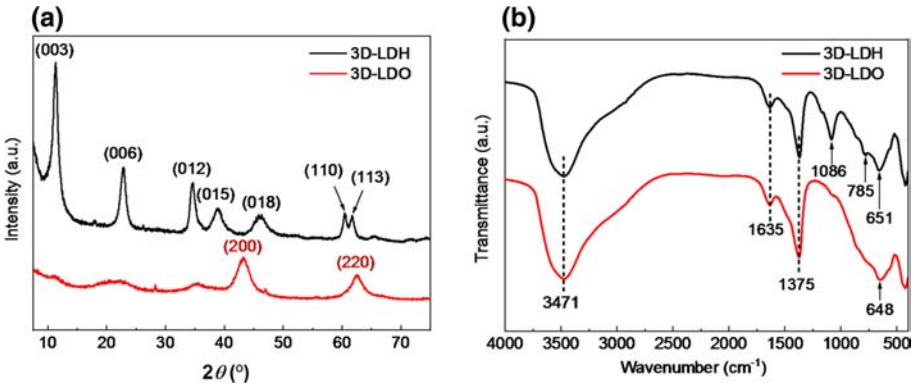

Fig. 1 **a** XRD patterns and **b** FT-IR spectra of 3D-LDH and 3D-LDO

and high crystallinity. Interestingly, the XRD pattern of the adsorbent changed remarkably after calcination. In detail, all characteristic peaks of 3D-LDH disappeared and two broad peaks located at 43.2° and 62.5° were found in the spectrum of 3D-LDO; these peaks could, respectively, be indexed to the (200) and (220) planes and indicate that the structure of 3D-LDH was destroyed by the elimination of interlayer CO_3^{2-} and water molecules during calcination. The (200) and (220) peaks reflect the presence of a MgO-like phase or magnesia–alumina solid solution, thus suggesting the formation of the metal oxide [40].

The FT-IR spectra of 3D-LDH and 3D-LDO are revealed in Fig. 1b. The broad absorption band at approximately 3471 cm^{-1} was assigned to the stretching vibrations of hydroxyl groups (OH^-) in layer and interlayer water molecules [41]. The weak peak at 1635 cm^{-1} was ascribed to the H–O–H bending vibrations of adsorbed water molecules [42]. The strong peak at 1375 cm^{-1} was caused by the antisymmetric stretching vibrations of CO_3^{2-} in the interlayer [43]. This band could also be observed in the FT-IR spectrum of 3D-LDO despite the removal of interlayer CO_3^{2-} after calcination at high temperature, and the crystal structure of 3D-LDH was destroyed (Fig. 1a), indicating that the interlayer carbonate anions and bound water were remaining. The previous reports pointed out that the anionic species remove completely only at temperature higher than 700 °C [25]. The bands at 785, 651, and 648 cm^{-1} were attributed to lattice vibrations, which mainly correspond to the bending vibrations of M–OH and stretching vibrations of M–O–M (M = Mg or Al) [44].

SEM images of 3D-LDH and 3D-LDO are depicted in Fig. 2. 3D-LDH (Fig. 2a) and 3D-LDO (Fig. 2b) presented 3D hierarchical flower-like morphologies with a uniform and orderly lamellar structure. The only difference between the structures of these materials is that the lamellar structure of 3D-LDO is looser than that of 3D-LDH, which could be attributed to the removal of CO_3^{2-} and OH^- in the interlayers of the adsorbent after calcination. These results indicate that the structure of 3D-LDH has high stability even at high temperature.

Changes in morphology over different synthesis times were monitored by SEM to further understand the formation mechanism of 3D-LDH. In Fig. 3a, the γ-Al_2O_3 particles were dispersed and present a loose state after ultrasound treatment. After 1 h of double-drop processing, the LDH lamellae grew and self-assembled to form a 3D flower-shaped spherical multi-level morphology; at this point, the superstructure of LDH presented texture (Fig. 3b). The layered structure densified and grew fully after aging for 15 h, and the size of the LDH lamellae increased. Finally, 3D hierarchical flower-like LDH was achieved (Fig. 3c).

According to the results described above (Fig. 3) and previous work by our research group [39], the morphology of 3D-LDH is controlled by its synthetic parameters, including synthetic time, amount of γ-Al_2O_3 support, molar ratio of Mg^{2+} and Al^{3+}, and pH. In the present experiment, 3D-LDH with a hierarchical microstructure was successfully synthesized through the following process. First, hydrolysis of γ-Al_2O_3 in an alkaline environment enables the formation of heterogeneous nucleation sites. Second, $Al(OH)_3$ initially precipitates along nucleation sites on the surface of γ-Al_2O_3 and forms an embryonic core of petals. Continuous addition of metal cations accumulates $Al(OH)_3$ and $Mg(OH)_2$ precipitates and

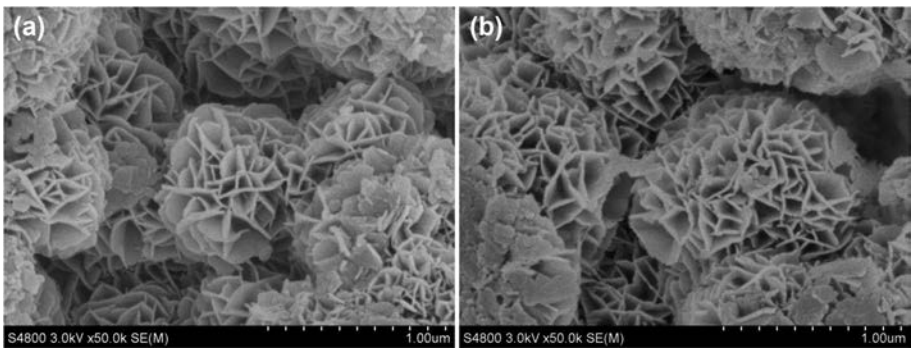

Fig. 2 SEM images of **a** 3D-LDH and **b** 3D-LDO

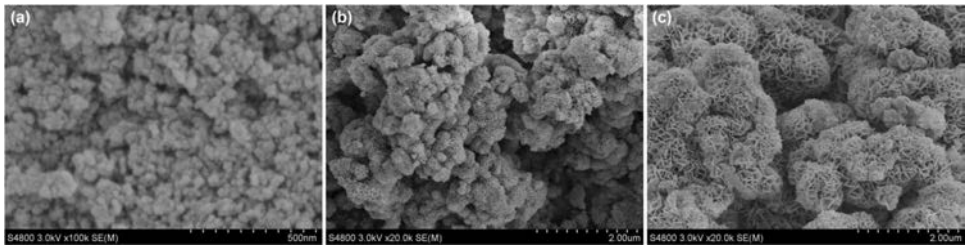

Fig. 3 Formation process of 3D-LDH at different synthetic times. SEM images of the sample obtained **a** 30 min after γ-Al_2O_3 ultrasonic treatment, **b** 1 h after double-drop process, and **c** after aging for 15 h

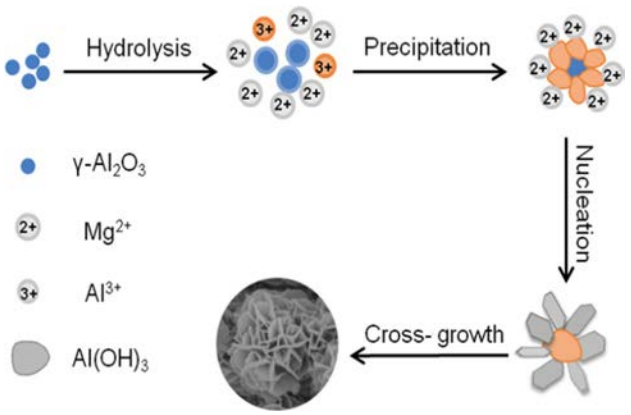

Fig. 4 Schematic of the formation mechanism of 3D-LDH

enhances the growth of LDH grains into a regular lamellar structure, thus forming a 3D hierarchical flower-like structure through cross-growth. Indeed, 3D-LDH grows via a self-assembly process that tends to develop spontaneously from the lowest energy state, thereby leading to the development of a lamellar, flower-like structure (Fig. 4).

The N_2 adsorption–desorption isotherms and corresponding pore size distribution curves of 3D-LDH and 3D-LDO are shown in Fig. 5. Both materials displayed the typical characteristics of type IV isotherms with clear hysteresis loops at high pressure, thus suggesting that the samples have a mesoporous structure. The BJH pore size distributions of the samples exhibited a uniform distribution of mesopores. Moreover, the specific surface area of the sample increased from 74.9 m^2/g to 204.2 m^2/g, the pore volume increased from 0.308 cm^3/g to 0.707 cm^3/g, and the average pore diameter decreased from 21.51 nm to 14.24 nm after calcination of 3D-LDH at 500 °C (Table 1).

The XRD, FT-IR, SEM, and BET results indicated that synthesizing 3D hierarchical flower-like layered double hydroxides via one-step double-drop coprecipitation method is completely feasible. Moreover, the resulting 3D-LDO has a higher specific surface area and larger pore volume than 3D-LDH, thereby rendering it suitable for use as an effective adsorbent for organic anionic dyes.

Table 1 Textural properties of the as-prepared samples

Samples	S^a_{BET} (m^2/g)	V^b_p (cm^3/g)	D^c_{av} (nm)
3D-LDH	74.9	0.308	21.51
3D-LDO	204.2	0.707	14.24

[a]BET surface area

[b]Pore volume

[c]Average pore size

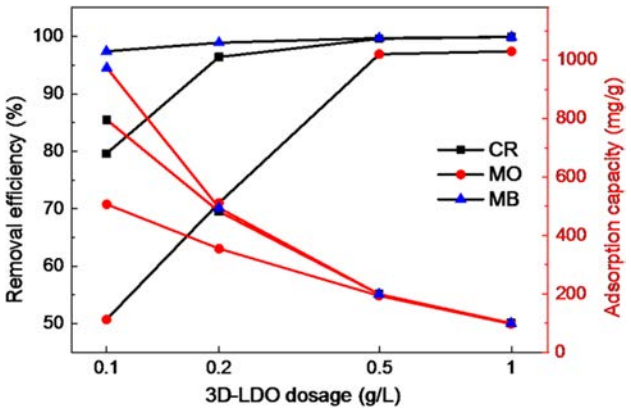

Fig. 6 Effect of adsorbent dosage for the adsorption of CR, MO and MB onto 3D-LDO

Effect of Key Parameters on the Adsorption Performance of 3D-LDO

The adsorbent dosage should be optimized to improve cost efficiency. In this experiment, different masses of 3D-LDO (i.e., 5, 10, 25, and 50 mg) were added to 50 mL of dye solution containing 100 mg/L CR, MO, or MB and mixed for 8 h at 25 °C. The removal efficiencies of the three dyes are shown in Fig. 6; increases in 3D-LDO adsorbent dosage increased the removal efficiency and decreased the relative adsorption capacity. The removal efficiency remarkably increased from 79% to 99.6% for CR and from 51% to 96.7% for MO as the 3D-LDO dosage increased from 0.1 g/L to 0.5 g/L. A subtle increase

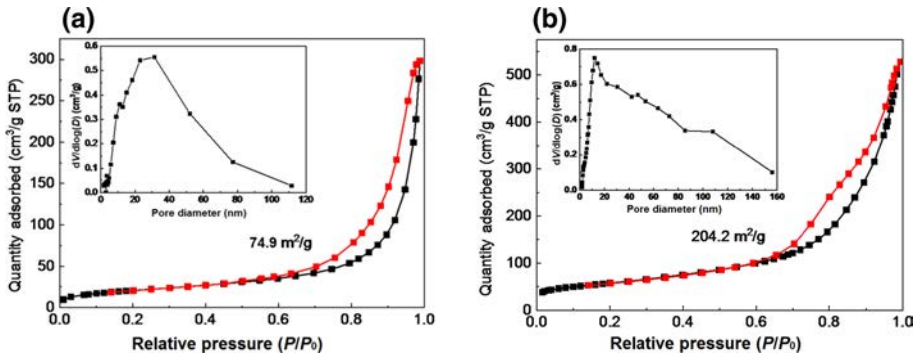

Fig. 5 N_2 adsorption–desorption isotherms and the corresponding BJH pore size distribution curves of **a** 3D-LDH and **b** 3D-LDO

in the removal efficiency of MB from 97% to 99.7% was observed under the same conditions, which implies that 3D-LDO has different adsorption capacities for CR, MO, and MB. The removal efficiencies of the three dyes did not significantly increase when the adsorbent dosage exceeded 0.5 g/L. Thus, considering cost and efficiency, the 3D-LDO dosage was set to 0.2 g/L for CR and MB and 0.5 g/L for MO in subsequent experiments.

The effect of initial dye concentration is displayed in Fig. 7. As the dye concentration increased from 50 mg/L to 300 mg/L, the removal efficiency decreased but the adsorption capacity increased. For example, as the dye concentration increased from 50 mg/L to 300 mg/L, the removal efficiencies for CR and MO onto 3D-LDO decreased from 97.2% to 81% and from 96.9% to 72.5%, respectively. But the adsorption capacity for CR and MO increased from 243.1 mg/g to 1190.1 mg/g and from 97.9 mg/g to 430.0 mg/g, respectively. When the initial dye concentration exceeded 200 mg/L, the removal efficiencies for CR and MO decreased significantly and the adsorption capacity gradually leveled off. By comparison, the removal efficiency for MB indicated a subtle decrease from 99.3% to 95.1%, thus showing that the adsorbent maintains good adsorption performance. These results confirm that 3D-LDO has different adsorption capacities for the three dyes. Specifically, 3D-LDO has much greater capacity for adsorbing MB than for adsorbing CR and MO.

Adsorption Kinetics

As shown in Fig. 8, the adsorption rates of the three anionic dyes by 3D-LDO occurred very quickly within the first 15 min of exposure. Thereafter, the adsorption capacity continued to increase at a relatively slow speed until a state of adsorption equilibrium was reached at 120 min. Thus, the adsorption time was set to 120 min in subsequent experiments. The higher the initial dye concentration, the longer the time required to reach adsorption equilibrium. The adsorption capacities of 3D-LDO for CR and MB were clearly significantly higher than that for MO. The experimental results were fitted to the pseudo-first-order, pseudo-second-order, and intraparticle diffusion kinetic models to further understand the dynamic characteristics of adsorption of the three dyes. The fitting results and corresponding kinetic parameters are shown in Figs. 9 and 10 and Tables 2 and 3.

The equations of the pseudo-first-order, pseudo-second-order, and intraparticle diffusion kinetic models are expressed as follows: Pseudo-first-order model:

$$\lg(q_e - q_t) = \lg q_e - \frac{k_1}{2.303}t \tag{4}$$

Pseudo-second-order model:

$$\frac{t}{q_t} = \frac{1}{k_2 q_e^2} + \frac{1}{q_e}t \tag{5}$$

Intraparticle diffusion kinetic model:

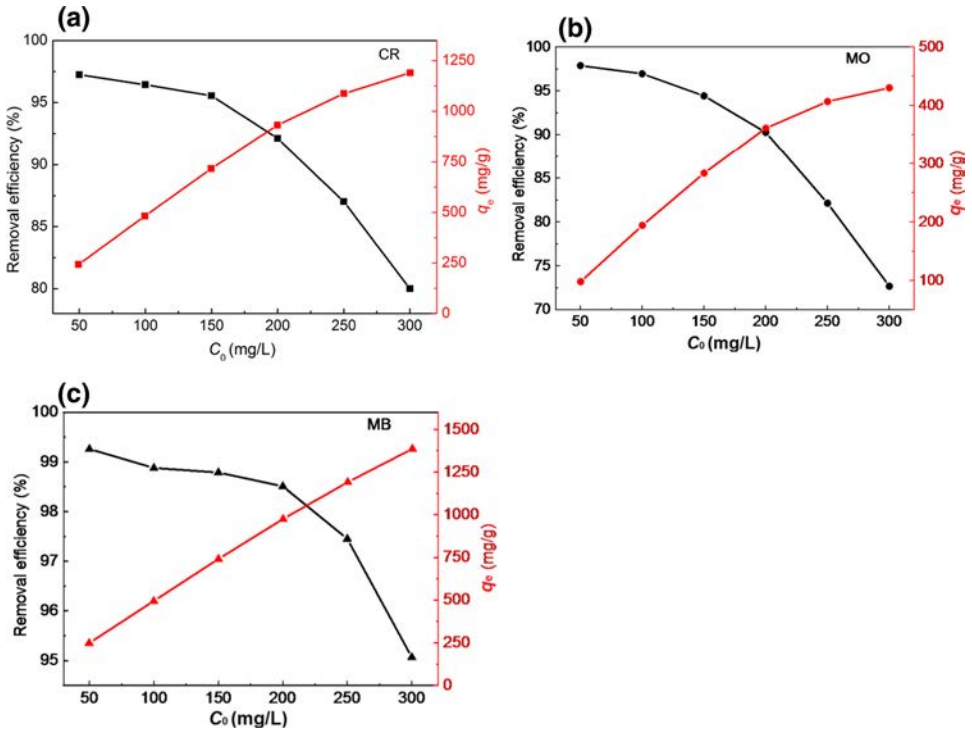

Fig. 7 Effect of initial dye concentrations on the adsorption of **a** CR, **b** MO and **c** MB onto 3D-LDO (25 °C, adsorbent dosage: 0.2 g/L for CR and MB, 0.5 g/L MO, contact time: 8 h)

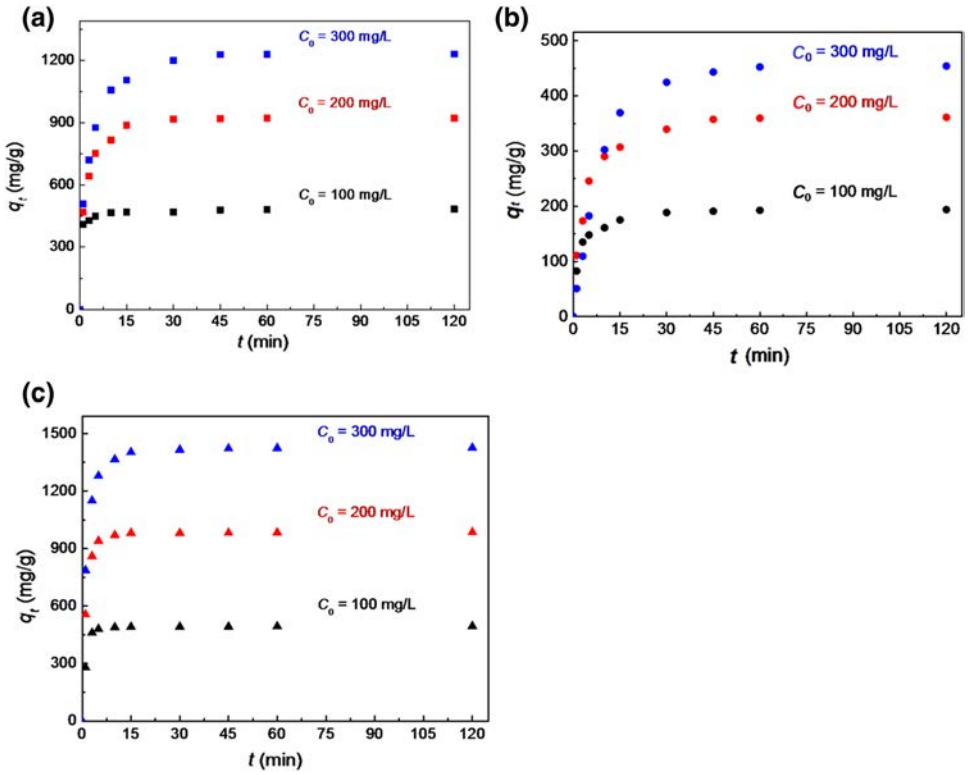

Fig. 8 Effect of contact time for the adsorption of **a** CR, **b** MO and **c** MB onto 3D-LDO

$$q_t = k_i t^{1/2} + C \tag{6}$$

where q_e is the calculated equilibrium adsorption capacity (mg/g), k_1 is the rate constant of the pseudo-first-order kinetic model, min^{-1}; k_2 is the rate constant of the pseudo-second-order kinetic model, g/(mg min); k_i is the intraparticle diffusion rate constant, mg/(g $min^{1/2}$); and C is a constant related to the thickness and boundary layer of the adsorbent.

The linear fitting curves and correlation coefficients (R^2) of the pseudo-first-order and second-order kinetic models in Fig. 9 and Table 2 reveal that the pseudo-second-order model fits the experimental data well, and, therefore, this kinetic model can describe the adsorption process of the dyes by 3D-LDO. Moreover, the equilibrium adsorption amounts ($q_{e,cal}$) calculated on the basis of the pseudo-second-order model are fairly close to the experimental values ($q_{e,exp}$). The results above indicate that dye adsorption by 3D-LDO is mainly dominated by chemical adsorption, which means chemical bonds are formed between the dye molecules and adsorbent [45–48]. The adsorption results were analyzed by using the intraparticle diffusion kinetic model to further describe the relevant diffusion mechanism. As revealed in Fig. 10 and Table 3, the complete adsorption process can be divided into three stages. First, the adsorption rate is very high, and adsorption mainly occurs through external diffusion. Next, the adsorption rate decreases because of the molecules adsorbed onto the internal pores of the adsorbent by particle diffusion. Finally, dynamic equilibrium adsorption is observed. All of the results thus far suggest that external diffusion and intraparticle diffusion severely affect the adsorption of dyes onto 3D-LDO [2, 49].

Adsorption Isotherms

The Langmuir and Freundlich isotherms were applied to analyze the adsorption results. The two models can be expressed as follows:Langmuir isotherm model:

$$\frac{C_e}{q_e} = \frac{1}{q_m K_L} + \frac{C_e}{q_m} \tag{7}$$

Freundlich isotherm model:

$$\ln q_e = \frac{1}{n} \ln C_e + \ln K_F \tag{8}$$

where q_m represent the maximum adsorption capacity, mg/g; K_L is a Langmuir constant; K_F and n are Freundlich constants.

The essential characteristics of the Langmuir isotherm can be expressed in terms of a dimensionless constant, called separation factor (R_L) [50], it can be obtained from the Langmuir isotherm model, and n can be obtained from the Freundlich isotherm model. The values of R_L and n are used to determine the feasibility of an adsorption process; specifically, $0 < R_L < 1$ and $2 < 1/n < 10$ indicate favorable adsorption. R_L is calculated as follows:

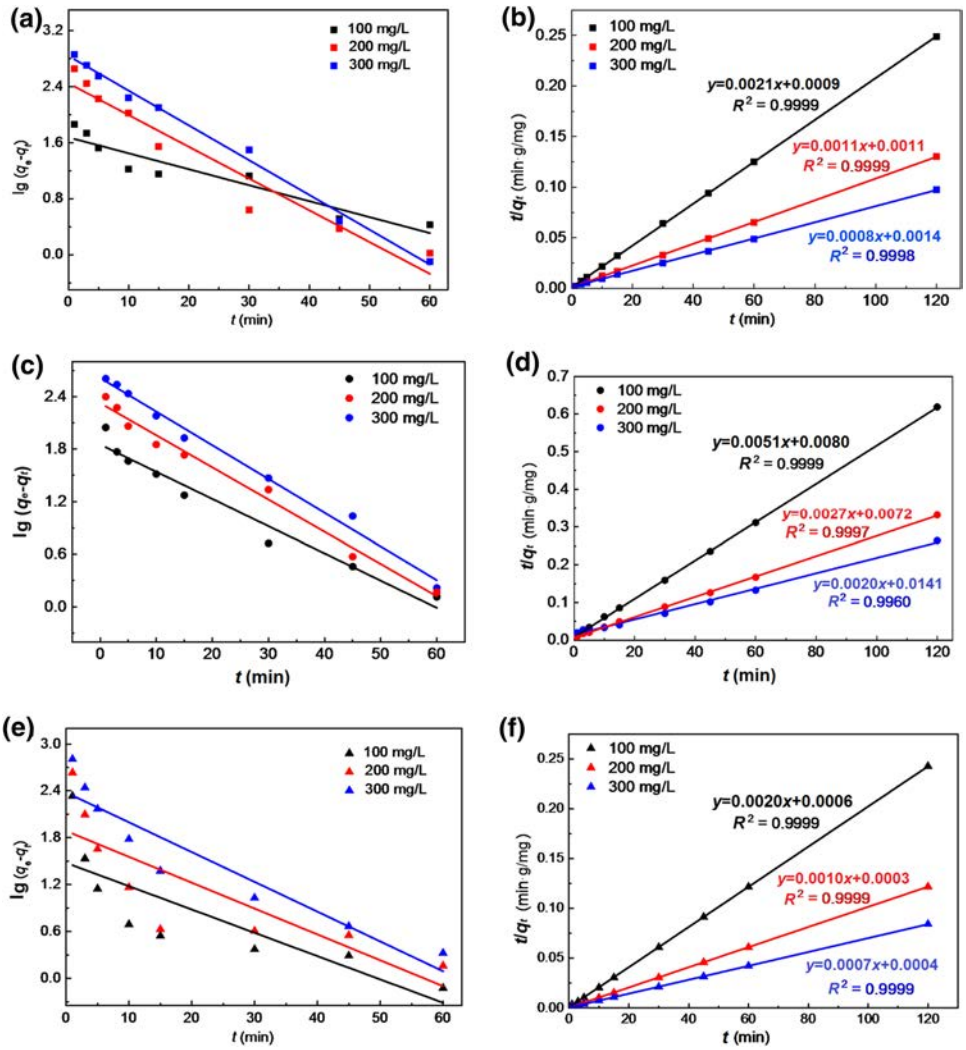

Fig. 9 Fitted results for **a, b** CR, **c, d** MO and **e, f** MB adsorption onto 3D-LDO by linearized pseudo-first order and pseudo-second order kinetic models

$$R_L = \frac{1}{1 + K_L C_0} \tag{9}$$

The adsorption isotherms and corresponding fitted straight lines are shown in Fig. 11, and the related parameters are listed in Table 4.

The fitted straight lines (Fig. 11) and related parameters (Table 4) reveal that the adsorption isotherms of the three dyes could be well represented by the Langmuir isotherm model. The R^2 of the Langmuir isotherm model was larger than that of the Freundlich isotherm model, thereby indicating that the adsorption of the three anionic dyes by 3D-LDO occurs via a monomolecular mechanism that allows only one layer of adsorbate molecules to be adsorbed onto the adsorbent surface [20]. Moreover, the R_L and n obtained demonstrate that the adsorption of the three dyes onto 3D-LDO is favorable in an available condition. The maximum adsorption capacities of 3D-LDO for CR, MO, and MB were calculated on the basis of the Langmuir isotherm model to be 1428.6, 476.2, and 1666.7 mg/g, respectively.

A comparison of the maximum adsorption capacities of 3D-LDO and other reported adsorbents for CR, MO, and MB is provided in Table 5. The adsorption capacities of 3D-LDO for CR, MO, and MB are clearly higher than those of previously reported materials. Thus, 3D-LDO is an excellent adsorbent for removing anionic dyes from aqueous solutions.

Adsorption Mechanism

We carried out detailed characterizations, including XRD, FT-IR, and SEM, to gain insights into the adsorption mechanism and assess the composition, structure, and morphology of 3D-LDO after adsorption CR, MO, and MB.

The zeta potentials of 3D-LDO at different pH are displayed in Fig. 12. The surface electrical properties of the adsorbent changed from positive to negative with increasing pH from 3 to 5, and the isoelectric point (pH_{zpc}) of 3D-LDO was 4.04, which means the adsorbent exhibits negative electrical properties at pH over 4.04. The adsorptions of

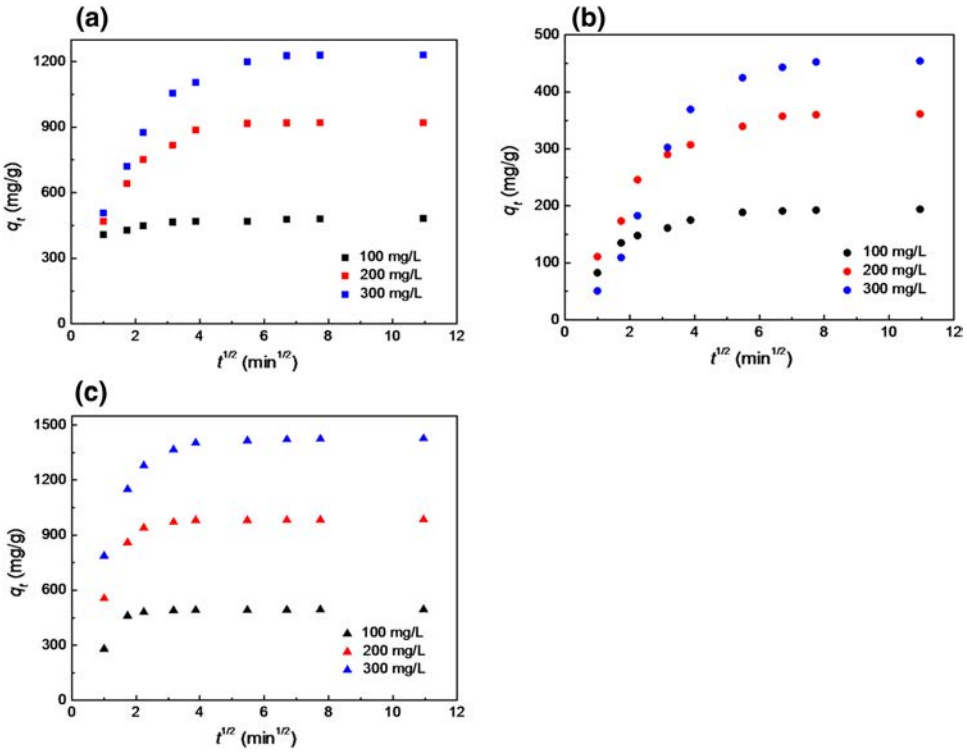

Fig. 10 The intraparticle diffusion kinetics for the adsorption of **a** CR, **b** MO and **c** MB

Table 2 Pseudo-first and pseudo-second-order kinetic parameters for adsorption of different dyes onto 3D-LDO

Dye	C_0 (mg/L)	Pseudo-first-order				Pseudo-second-order		
		$q_{e,exp}$	$q_{e,cal}$	k_1	R^2	$q_{e,cal}$	k_2	R^2
CR	100	482.2	47.58	0.0525	0.8803	476.2	0.0049	0.9999
	200	921.2	281.38	0.1046	0.9322	909.1	0.0011	0.9999
	300	1230.1	693.43	0.1145	0.9918	1250.0	0.00046	0.9998
MO	100	193.9	71.02	0.0714	0.9578	196.1	0.0033	0.9999
	200	361.1	211.80	0.0845	0.9846	370.4	0.0010	0.9997
	300	454.0	352.50	0.0654	0.9693	490.2	0.0003	0.9960
MB	100	494.4	30.10	0.0686	0.6217	497.8	0.0067	0.9999
	200	985.1	77.09	0.0762	0.6413	990.1	0.0034	0.9999
	300	1426.0	239.39	0.0877	0.8755	1428.6	0.0012	0.9999

Table 3 Intraparticle diffusion model constants and correlation coefficients for CR, MO, and MB adsorption onto 3D-LDO

Dye	C_0 (mg/L)	Intraparticle diffusion model parameters								
		k_{d1}	k_{d2}	k_{d3}	C_1	C_2	C_3	R_1^2	R_2^2	R_3^2
CR	100	31.66	1.27	0.7805	376.09	462.21	473.72	0.9818	0.7767	0.9957
	200	228.91	39.44	0.4998	241.83	708.47	915.83	0.9996	0.8188	0.8835
	300	297.27	61.17	0.5982	208.6	864.44	1223.8	0.9997	0.9987	0.7266
MO	100	54.11	11.26	0.6136	32.239	128.03	187.31	0.9475	0.9478	0.8869
	200	107.4	21.15	0.7814	-1.2347	223.93	352.74	0.9784	0.9982	0.8434
	300	113.16	22.783	1.7578	-60.703	275.78	434.78	0.9957	0.9745	1.0000
MB	100	246.99	6.61	0.4378	32.36	466.48	489.76	1	0.8979	0.9016
	200	415.89	25.41	0.7659	139.56	885.2	976.92	1	0.9607	0.9114
	300	405.07	19.23	0.9862	400.99	1314.1	1415.4	0.974	0.7804	0.8888

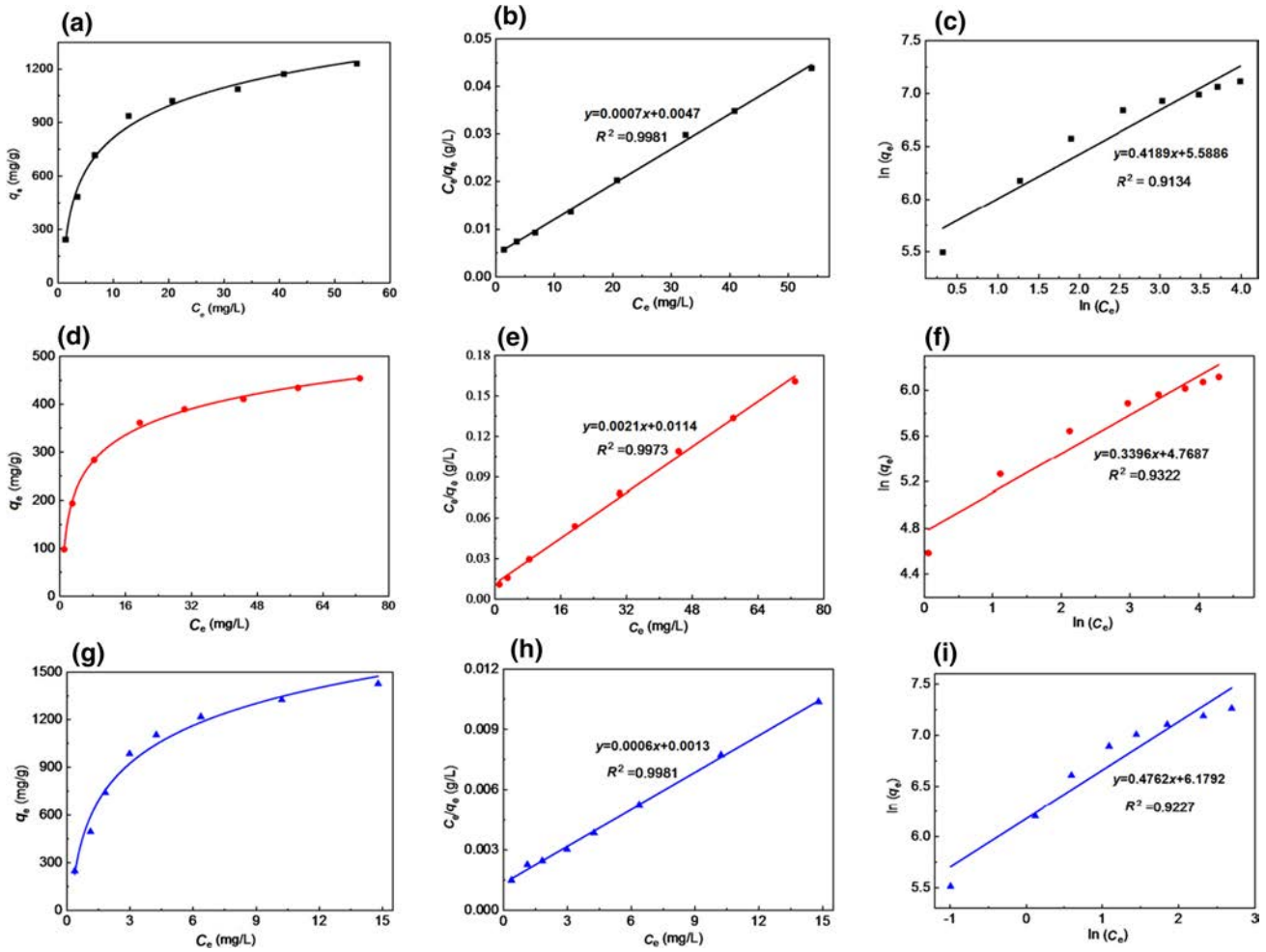

Fig. 11 Adsorption isotherms, Langmuir isotherm and Freundlich isotherm models of **a**, **b**, **c** CR, **d**, **e**, **f** MO and **g**, **h**, **i** MB adsorbed by 3D-LDO

Table 4 Parameters of Langmuir and Freundlich isotherm models for adsorption of CR, MO, and MB onto 3D-LDO

Dye	Langmuir isotherm model				Freundlich isotherm model		
	q_m(mg/g)	K_L	R_L	R^2	K_F	n	R^2
CR	1428.6	0.1489	0.0219–0.1184	0.9981	267.4	2.387	0.9134
MO	476.2	0.1842	0.0178–0.0979	0.9973	117.8	2.945	0.9322
MB	1666.7	0.4615	0.0072–0.0415	0.9981	482.6	2.100	0.9227

dyes onto 3D-LDO under different initial pH are shown in Fig. 13. Whereas the removal efficiencies of 3D-LDO for CR and MO decreased with increasing initial pH, its removal efficiency for MB increased. CR, MO, and MB are similarly anionic dyes, but the latter contains a positive charged group (=N^+H–) that could interact with the negatively charged adsorbent at pH > pH_{zpc} [54]. Thus, electrostatic attraction is crucial for the adsorption of MB onto 3D-LDO. The memory effect of 3D-LDO also appeared to play a significant role in the adsorption process. The XRD patterns of 3D-LDO before and after dye adsorption are shown in Fig. 14. Here, the structure of hydrotalcite in 3D-LDO appeared to be reconstructed after dye adsorption. Specifically, the XRD patterns of 3D-LDO after dye adsorption contained characteristic peaks similar to those corresponding to hydrotalcite-like crystalline structures, including those at 11.3°, 22.8°, 34.7°, and 60.5°, which were, respectively, indexed to the (003), (006), (012), and (110) planes of the LDH [55]. Moreover, the structural data calculated by XRD analysis (Table S2) revealed that the interlayer distance of 3D-LDO after dye adsorption is greater than that of 3D-LDH. Thus, because the dye molecules are larger than CO_3^{2-} and OH^-,

Table 5 Maximum adsorption capacities of 3D-LDO and other adsorbents

Adsorbents	T (°C)	q_{max} (mg/g)			References
		CR	MO	MB	
3D-LDO	25	1428.6	476.2	1666.7	This work
Mg–Al-CO_3 LDH	25	934.43	–	–	[2]
Fe_3O_4@Mg–Al LDH	–	813.0	–	–	[9]
NiCo-LDH	30	909.2	–	–	[20]
γ-AlO(OH)/Mg–Al-LDH/C	22	477	–	–	[27]
His-LDH	25	1112	–	–	[51]
GO-NiFe LDH	30	489	438	–	[14]
MgNiAl-C	25 ± 1	–	375.4	–	[25]
O_3D-LDH	25	–	377.89	–	[30]
Hollow MgFe-LDO	~25	–	–	398	[31]
Mg_3Al LDO	45	–	–	138.9	[52]
Porous Al_2O_3 microspheres	~25	–	–	1588	[53]

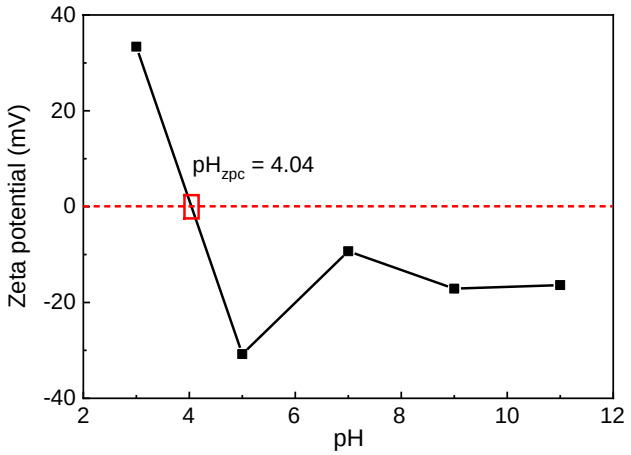

Fig. 12 Zeta potential of 3D-LDO at different pH

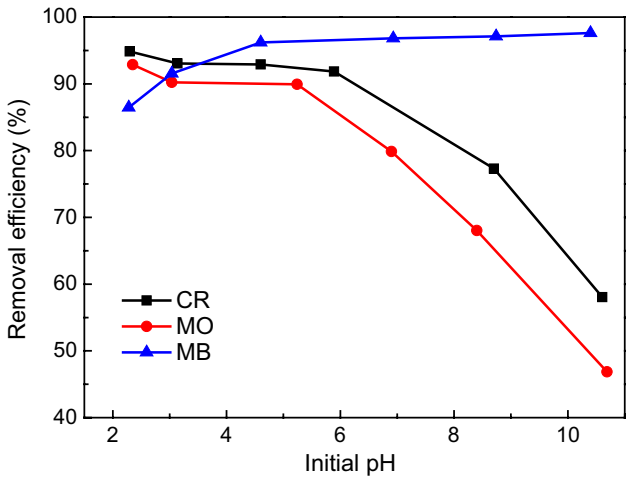

Fig. 13 Effect of initial pH on the adsorption of CR, MO, and MB onto 3D-LDO

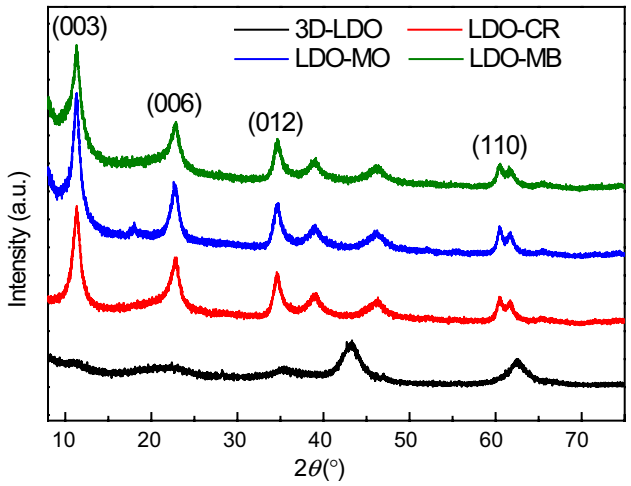

Fig. 14 XRD patterns of 3D-LDO before and after adsorption of CR, MO, and MB

part of the dye molecules may be intercalated into the interlamellar space of the reconstructed hydrotalcite during the adsorption process. SEM images of 3D-LDO after dye adsorption are shown in Fig. 15; the images obtained further demonstrate that the structure of 3D-LDO is reconstructed to form a hydrotalcite-like structure during adsorption. In the figure, all presented a cross-stack of sheet structures with some degree of aggregation, which results in a decrease in specific surface area and available active adsorption sites. As a result, the removal efficiency of the dye by the recycled 3D-LDO adsorbent decreased.

FT-IR spectral analysis was performed to understand the adsorption mechanism of 3D-LDO for the three anionic dyes, and the results are revealed in Fig. 16. The spectrum of 3D-LDO + CR showed characteristic peaks at 1176, 1118, and 1043 cm^{-1}, which were associated with the asymmetric and symmetric stretching vibrations of the sulfonate group ($–SO_3^-$) of CR molecules [56, 57]. The spectrum of 3D-LDO + MO showed bands at 1604, 1521, 1124, and 1036 cm^{-1}, which were attributed to the vibrations C=C, N=N, and C–N and the stretching vibrations of the sulfonic acid group ($–SO_3^-$) of MO, respectively [58]. The band at 1006 cm^{-1} was assigned to the C–H in-plane bending vibrations of benzene rings. The spectrum of 3D-LDO + MB revealed characteristic peaks at 1174 and 1036 cm^{-1}, which were attributed to the asymmetric and symmetric stretching vibrations of the $–SO_3^-$ group of MB. These results confirm that the three anionic dyes were successfully adsorbed onto the surface of 3D-LDO and that the anionic dyes molecules

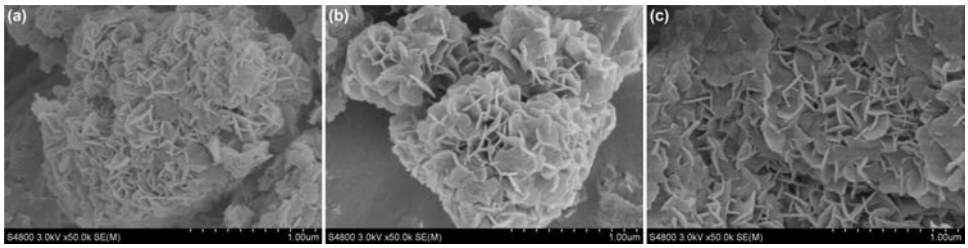

Fig. 15 SEM images of 3D-LDO after adsorption of **a** CR, **b** MO and **c** MB

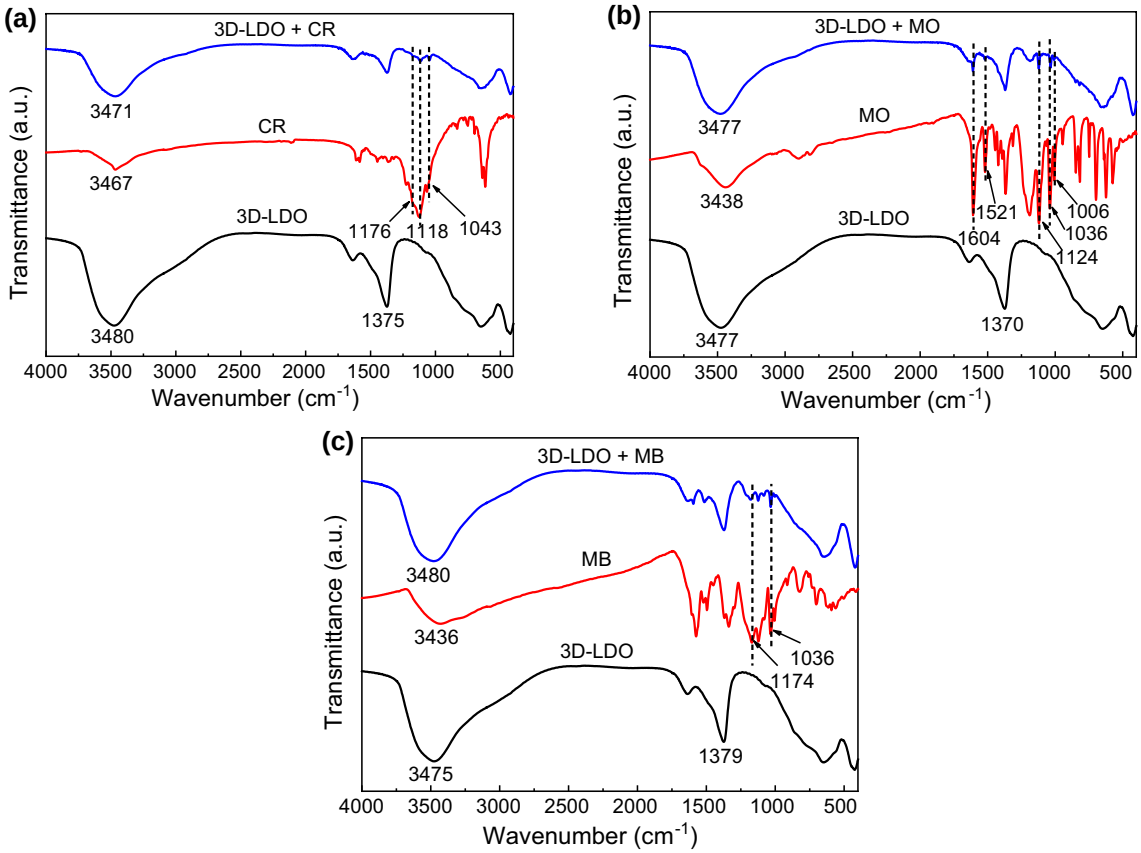

Fig. 16 FT-IR spectra of three anionic dyes and 3D-LDO before and after adsorption

replaced part of the CO_3^{2-} and entered the LDH layer during the structural reconstruction process.

The superior adsorption performance of 3D-LDO may be attributed to not only its surface adsorption and the memory effect of LDO but also its unique 3D hierarchical flower-like structure [31]. To confirm whether the structure of the proposed adsorbent contributes to its performance, we synthesized conventional MgAl-LDO with a hexagonal plate-like morphology and applied it to the adsorption of CR, MO, and MB under the same conditions. As shown in Fig. 17, the removal efficiency of 3D-LDO was higher than that of ordinary MgAl-LDO. This finding can be ascribed to the hierarchical flower-like structure of 3D-LDO, which provides an abundance of microchannels and exposes more active sites to enhance mass transfer and adsorption [31]. By contrast, ordinary MgAl-LDO exhibited sheet stacking and aggregation, which leads to lower specific surface areas and fewer active sites exposed for adsorption. These findings are confirmed by SEM images in Fig. S1 and Table S3.

According to the above analysis, the excellent adsorption performance of 3D-LDO is determined by not only the memory effect of LDO and surface adsorption but also the hierarchical flower-like structure of the adsorbent. This structure features a large specific surface area and exposes abundant active sites for adsorption.

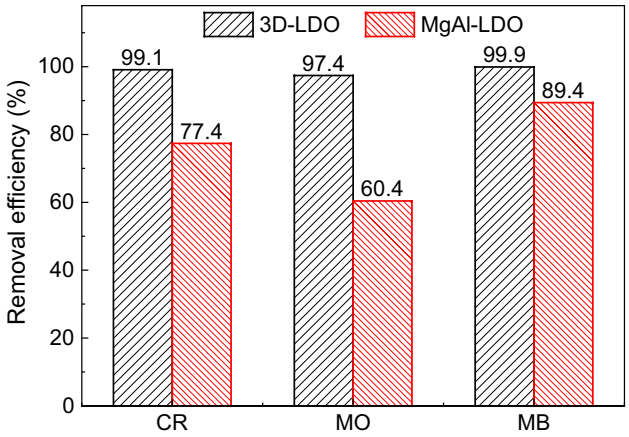

Fig. 17 Removal efficiency of three dyes by 3D-LDO and conventional MgAl-LDO

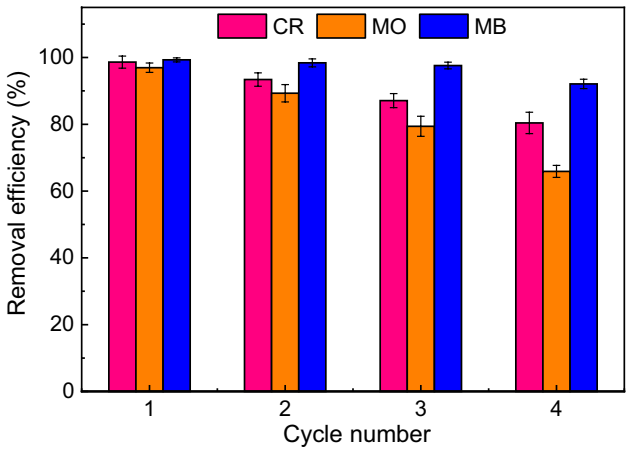

Fig. 18 Reusability of 3D-LDO for CR, MO, and MB adsorption

Recycle Performance

The recyclability of an adsorbent is an important consideration for its practical application. In this study, 3D-LDO was separated from the mixture solution after adsorption, dried at 80 °C for 6 h, and calcined at 500 °C for 3 h in a furnace. The reclaimed 3D-LDO was then used for the next experiment. The recycling performance of the regenerated 3D-LDO is displayed in Fig. 18. The removal efficiencies of the adsorbent for CR, MO, and MB slightly decreased with increasing number of recycle but were eventually maintained at 80.4%, 65.9%, and 92.1%, respectively, after four cycles. This result suggests that 3D-LDO has satisfactory recyclability for anionic dyes, especially MB. This phenomenon could be explained from two perspectives. On the one hand, the adsorption sites of 3D-LDO are not completely released because of dye residues occupying these sites after calcination. On the other hand, the layered structure of the LDO may collapse and be unable to return to its original lamellar shape after multiple calcinations, thereby resulting in a decrease in specific surface area, fewer available active adsorption sites, and lower removal efficiency. SEM images of 3D-LDO obtained after four recycles (Fig. S2) confirm these results.

Conclusions

In summary, hierarchical flower-like 3D-LDH was successfully synthesized via a simple double-drop coprecipitation method. The γ-Al_2O_3 template played a key role in forming the hierarchical structure of the adsorbent. The calcined product 3D-LDO exhibited excellent adsorption performance for organic anionic dyes, especially MB. The maximum adsorption capacity of 3D-LDO reached 1428.6, 476.2, and 1666.7 mg/g for CR, MO, and MB, respectively; such performance is superior to that of most previously reported adsorbents. The adsorption process of 3D-LDH could be well described by the pseudo-second-order kinetic and Langmuir isotherm models. The removal mechanism of the adsorbent for anionic dyes involved surface adsorption, the memory effect of LDO, and the 3D hierarchical microstructure of the material. In summary, this study described a facile and effective method to fabricate 3D-LDH via a green and environment-friendly approach without the use of organic solvents. The proposed method yielded an effective and sustainable adsorbent for organic anionic dye wastewater treatment.

Acknowledgements This study was supported by the National Key R&D Program of China (No. 2017YFB0602702-02).

References

1. Yang HW, Bai LJ, Wei DL et al (2019) Ionic self-assembly of poly(ionic liquid)-polyoxometalate hybrids for selective adsorption of anionic dyes. Chem Eng J 358:850–859
2. Zhang WK, Liang Y, Wang JW et al (2019) Ultrasound-assisted adsorption of Congo red from aqueous solution using $MgAlCO_3$ layered double hydroxide. Appl Clay Sci 174:100–109
3. Ling FL, Fang L, Lu Y et al (2016) A novel CoFe layered double hydroxides adsorbent: high adsorption amount for methyl orange dye and fast removal of Cr(VI). Microporous Mesoporous Mater 234:230–238
4. Lau WJ, Ismail AF (2009) Polymeric nanofiltration membranes for textile dye wastewater treatment: preparation, performance evaluation, transport modelling, and fouling control: a review. Desalination 245(1–3):321–348
5. Ma X, Chen PL, Zhou M et al (2017) Tight ultrafiltration ceramic membrane for separation of dyes and mixed salts (both NaCl/Na_2SO_4) in textile wastewater treatment. Ind Eng Chem Res 56(24):7070–7079

6. Cotillas S, Llanos J, Cañizares P et al (2018) Removal of Procion Red MX-5B dye from wastewater by conductive-diamond electrochemical oxidation. Electrochim Acta 263:1–7
7. Türgay O, Ersöz G, Atalay S et al (2011) The treatment of azo dyes found in textile industry wastewater by anaerobic biological method and chemical oxidation. Sep Purif Technol 79(1):26–33
8. Zargari S, Rahimi R, Ghaffarinejad A et al (2016) Enhanced visible light photocurrent response and photodegradation efficiency over TiO_2–graphene nanocomposite pillared with tin porphyrin. J Colloid Interface Sci 466:310–321
9. Yao W, Yu SJ, Wang J et al (2017) Enhanced removal of methyl orange on calcined glycerol-modified nanocrystallined Mg/Al layered double hydroxides. Chem Eng J 307:476–486
10. Extremera R, Pavlovic I, Pérez MR et al (2012) Removal of acid orange 10 by calcined Mg/Al layered double hydroxides from water and recovery of the adsorbed dye. Chem Eng J 213:392–400
11. Lu L, Li J, Ng DHL et al (2017) Synthesis of novel hierarchically porous Fe_3O_4@MgAl–LDH magnetic microspheres and its superb adsorption properties of dye from water. J Ind Eng Chem 46:315–323
12. Patra S, Roy E, Madhuri R et al (2016) Agar based bimetallic nanoparticles as high-performance renewable adsorbent for removal and degradation of cationic organic dyes. J Ind Eng Chem 33:226–238
13. Yagub MT, Sen TK, Afroze S et al (2014) Dye and its removal from aqueous solution by adsorption: a review. Adv Colloid Interface Sci 209:172–184
14. Zheng YQ, Cheng B, You W et al (2019) 3D hierarchical graphene oxide-NiFe LDH composite with enhanced adsorption affinity to Congo red, methyl orange and Cr(VI) ions. J Hazard Mater 369:214–225
15. Demirbas A (2009) Agricultural based activated carbons for the removal of dyes from aqueous solutions: a review. J Hazard Mater 167(1–3):1–9
16. Zhou CJ, Wu QL, Lei TZ et al (2014) Adsorption kinetic and equilibrium studies for methylene blue dye by partially hydrolyzed polyacrylamide/cellulose nanocrystal nanocomposite hydrogels. Chem Eng J 251:17–24
17. Jin XY, Yu B, Chen ZL et al (2014) Adsorption of Orange II dye in aqueous solution onto surfactant-coated zeolite: characterization, kinetic and thermodynamic studies. J Colloid Interface Sci 435:15–20
18. Vimonses V, Lei SM, Jin B et al (2009) Kinetic study and equilibrium isotherm analysis of Congo Red adsorption by clay materials. Chem Eng J 148(2–3):354–364
19. Zeng SY, Duan SX, Tang RF et al (2014) Magnetically separable $Ni_{0.6}Fe_{2.4}O_4$ nanoparticles as an effective adsorbent for dye removal: synthesis and study on the kinetic and thermodynamic behaviors for dye adsorption. Chem Eng J 258:218–228
20. Hu HJ, Liu JY, Xu ZH et al (2019) Hierarchical porous Ni/Co-LDH hollow dodecahedron with excellent adsorption property for Congo red and Cr(VI) ions. Appl Surf Sci 478:981–990
21. Yu JY, Fan GL, Yang Y et al (2014) Multi-level three-dimensional Mg-Al layered double hydroxide hierarchical microstructures with enhanced basic catalytic property. J Colloid Interface Sci 432:1–9
22. Liu P, Derchi M, Hensen EJM (2013) Synthesis of glycerol carbonate by transesterification of glycerol with dimethyl carbonate over MgAl mixed oxide catalysts. Appl Catal A: Gen 467:124–131
23. dos Santos RMM, Gonçalves RGL, Constantino VRL et al (2017) Adsorption of Acid Yellow 42 dye on calcined layered double hydroxide: effect of time, concentration, pH and temperature. Appl Clay Sci 140:132–139
24. Baskaran T, Christopher J, Sakthivel A (2015) Progress on layered hydrotalcite (HT) materials as potential support and catalytic materials. RSC Adv 5(120):98853–98875
25. Zaghouane-Boudiaf H, Boutahala M, Arab L (2012) Removal of methyl orange from aqueous solution by uncalcined and calcined MgNiAl layered double hydroxides (LDHs). Chem Eng J 187:142–149
26. Li ZC, Yang BJ, Zhang SN et al (2014) A novel approach to hierarchical sphere-like ZnAl-layered double hydroxides and their enhanced adsorption capability. J Mater Chem A 2(26):10202
27. Li J, Zhang N, Ng DHL (2015) Synthesis of a 3D hierarchical structure of γ-AlO(OH)/Mg–Al-LDH/C and its performance in organic dyes and antibiotics adsorption. J Mater Chem A 3(42):21106–21115
28. Dong T, Zhang X, Li M et al (2018) Hierarchical flower-like Ni–Co layered double hydroxide nanostructures: synthesis and super performance. Inorg Chem Front 5(12):3033–3041
29. Xu J, Deng HH, Song JX et al (2017) Synthesis of hierarchical flower-like Mg_2Al–Cl layered double hydroxide in a surfactant-free reverse microemulsion. J Colloid Interface Sci 505:816–823
30. Zhang P, Ouyang SD, Li P et al (2019) Enhanced removal of ionic dyes by hierarchical organic three-dimensional layered double hydroxide prepared via soft-template synthesis with mechanism study. Chem Eng J 360:1137–1149
31. Zong YT, Li KT, Tian R et al (2018) Highly dispersed layered double oxide hollow spheres with sufficient active sites for adsorption of methyl blue. Nanoscale 10(48):23191–23197
32. Li L, Ma RZ, Iyi N et al (2006) Hollow nanoshell of layered double hydroxide. Chem Commun 29:3125
33. Li B, He J (2008) Multiple effects of dodecanesulfonate in the crystal growth control and morphosynthesis of layered double hydroxides. J Phys Chem C 112(29):10909–10917
34. He S, Zhao YF, Wei M et al (2012) Fabrication of hierarchical layered double hydroxide framework on aluminum foam as a structured adsorbent for water treatment. Ind Eng Chem Res 51(1):285–291
35. Shao MF, Ning FY, Zhao YF et al (2012) Core–shell layered double hydroxide microspheres with tunable interior architecture for supercapacitors. Chem Mater 24(6):1192–1197
36. Sun HX, Chu ZY, Hong DH et al (2016) Three-dimensional hierarchical flower-like Mg-Al-layered double hydroxides: fabrication, characterization and enhanced sensing properties to NO*x* at room temperature. J Alloyf Compd 658:561–568
37. Bo LF, Li QR, Wang YH et al (2016) Adsorptive removal of fluoride using hierarchical flower-like calcined Mg-Al layered double hydroxides. Environ Prog Sustain Energy 35(5):1420–1429
38. Yu XY, Luo T, Jia Y et al (2012) Three-dimensional hierarchical flower-like Mg–Al-layered double hydroxides: highly efficient adsorbents for As(v) and Cr(vi) removal. Nanoscale 4(11):3466
39. Sun YL, Gao X, Yang N et al (2019) Morphology-controlled synthesis of three-dimensional hierarchical flowerlike Mg–Al layered double hydroxides with enhanced catalytic activity for transesterification. Ind Eng Chem Res 58(19):7937–7947
40. Wu GD, Wang XL, Chen B et al (2007) Fluorine-modified mesoporous Mg-Al mixed oxides: mild and stable base catalysts for O-methylation of phenol with dimethyl carbonate. Appl Catal A: Gen 329:106–111
41. Nethravathi C, Viswanath B, Sebastian M et al (2010) Exfoliation of α-hydroxides of nickel and cobalt in water. J Colloid Interface Sci 345(1):109–115
42. Herrero M, Benito P, Labajos FM et al (2007) Nanosize cobalt oxide-containing catalysts obtained through microwave-assisted methods. Catal Today 128(3–4):129–137
43. Zheng YM, Li N, Zhang WD (2012) Preparation of nanostructured microspheres of Zn-Mg-Al layered double hydroxides with high adsorption property. Colloids Surf A: Physicochem Eng Asp 415:195–201

44. Kloprogge J, Frost RL (1999) Fourier transform infrared and Raman spectroscopic study of the local structure of Mg-, Ni-, and Co-hydrotalcites. J Solid State Chem 146(2):506–515
45. Pooralhossini J, Ghaedi M, Zanjanchi MA et al (2017) Ultrasonically assisted removal of Congo Red, Phloxine B and Fast green FCF in ternary mixture using novel nanocomposite following their simultaneous analysis by derivative spectrophotometry. Ultrason Sonochemistry 37:452–463
46. Cao CY, Liang CH, Yin Y et al (2017) Thermal activation of serpentine for adsorption of cadmium. J Hazard Mater 329:222–229
47. Zhang ML, Yao QF, Lu C et al (2014) Layered double hydroxide–carbon dot composite: high-performance adsorbent for removal of anionic organic dye. ACS Appl Mater Interfaces 6(22):20225–20233
48. Wu FC, Tseng RL, Juang RS (2009) Characteristics of Elovich equation used for the analysis of adsorption kinetics in dye-chitosan systems. Chem Eng J 150(2–3):366–373
49. Nethaji S, Sivasamy A, Mandal AB (2013) Preparation and characterization of corn cob activated carbon coated with nano-sized magnetite particles for the removal of Cr(VI). Bioresour Technol 134:94–100
50. Pourfaraj R, Fatemi SJ, Kazemi SY et al (2017) Synthesis of hexagonal mesoporous MgAl LDH nanoplatelets adsorbent for the effective adsorption of Brilliant Yellow. J Colloid Interface Sci 508:65–74
51. Shamsayei M, Yamini Y, Asiabi H (2018) Fabrication of zwitterionic histidine/layered double hydroxide hybrid nanosheets for highly efficient and fast removal of anionic dyes. J Colloid Interface Sci 529:255–264
52. Qiao Y, Li QR, Chi HJ et al (2018) Methyl blue adsorption properties and bacteriostatic activities of Mg-Al layer oxides via a facile preparation method. Appl Clay Sci 163:119–128
53. Li J, Xu L, Sun PP et al (2017) Novel application of red mud: facile hydrothermal-thermal conversion synthesis of hierarchical porous AlOOH and Al_2O_3 microspheres as adsorbents for dye removal. Chem Eng J 321:622–634
54. Sharma P, Hussain N, Borah DJ et al (2013) Kinetics and adsorption behavior of the methyl blue at the graphene oxide/reduced graphene oxide nanosheet–water interface: a comparative study. J Chem Eng Data 58(12):3477–3488
55. Hájek M, Kutálek P, Smoláková L et al (2015) Transesterification of rapeseed oil by Mg-Al mixed oxides with various Mg/Al molar ratio. Chem Eng J 263:160–167
56. Wang LX, Li JC, Wang ZT et al (2013) Low-temperature hydrothermal synthesis of α-Fe/Fe_3O_4nanocomposite for fast Congo red removal. Dalton Trans 42(7):2572–2579
57. Yang SX, Wang LY, Zhang XD et al (2015) Enhanced adsorption of Congo red dye by functionalized carbon nanotube/mixed metal oxides nanocomposites derived from layered double hydroxide precursor. Chem Eng J 275:315–321
58. Zhou QQ, Chen FF, Wu W et al (2016) Reactive orange 5 removal from aqueous solution using hydroxyl ammonium ionic liquids/layered double hydroxides intercalation composites. Chem Eng J 285:198–206

Na Yang is a lecturer of the School of Chemical Engineering and Technology, Tianjin University. Her research interests cover the area of biomimetic and biologically inspired membranes and membrane processes, mass transfer and separation engineering and chemical hydrodynamics.